Optimized Synthesis and Device Integration of Long 17-Atom-Wide Armchair Graphene Nanoribbons

Jeong Ha Hwang,[†,‡,¶¶] Nicolò Bassi,[†,¶¶] Mayada Fadel,[¶] Oliver Braun,[§,||] Tim Dumslaff,[⊥] Carlo A. Pignedoli,[†] Michael Stiefel,[§] Roman Furrer,[§] Hironobu Hayashi,[#] Hiroko Yamada,[@] Akimitsu Narita,[⊥] Klaus Müllen,[⊥] Michel Calame,[§,||,△] Mickael Perrin,[‡,§,∇] Roman Fasel,[†,††] Pascal Ruffieux,[†] Vincent Meunier,[‡‡] and Gabriela Borin Barin[*,†]

†*nanotech@surfaces Laboratory, Empa - Swiss Federal Laboratories for Materials Science and Technology, 8600 Dübendorf, Switzerland*

‡*Department of Information Technology and Electrical Engineering, ETH Zürich, 8092 Zürich, Switzerland*

¶*Department of Materials Science and Engineering, Rensselaer Polytechnic Institute, Troy, NY 12180, USA*

§*Transport at Nanoscale Interfaces Laboratory, Empa - Swiss Federal Laboratories for Materials Science and Technology, 8600 Dübendorf, Switzerland*

||*Department of Physics, University of Basel, 4056 Basel, Switzerland*

⊥*Max Planck Institute for Polymer Research, 55128 Mainz, Germany*

#*Center for Basic Research on Materials, National Institute for Materials Science (NIMS), 1-2-1 Sengen, Tsukuba, Ibaraki 305-0047, Japan*

@*Kyoto University, Kyoto, 606-8501, Japan*

△*Swiss Nanoscience Institute, University of Basel, 4056 Basel, Switzerland*

∇*Quantum Center, ETH Zürich, 8093 Zürich, Switzerland*

††*Department of Chemistry, Biochemistry and Pharmaceutical Sciences, University of Bern, 3012 Bern, Switzerland*

‡‡*Department of Engineering Science and Mechanics, Pennsylvania State University, University*

Abstract

Seventeen-carbon-atom-wide armchair graphene nanoribbons (17-AGNRs) are promising candidates for high-performance electronic devices due to their narrow electronic bandgap. Atomic precision in edge structure and width control is achieved through a bottom-up on-surface synthesis (OSS) approach from tailored molecular precursors in ultra-high vacuum (UHV). This synthetic protocol must be optimized to meet the structural requirements for device integration, with ribbon length being the most critical parameter. Here, we report optimized OSS conditions that produce 17-AGNRs with an average length of approximately ~17 nm. This length enhancement is achieved through a gradual temperature ramping during an extended annealing period, combined with a template-like effect driven by monomer assembly at high surface coverage. The resulting 17-AGNRs are comprehensively characterized in UHV using scanning probe techniques and Raman spectroscopy. Raman measurements following substrate transfer enabled the characterization of GNRs' length distribution on the device substrate and confirmed their stability under ambient conditions and harsh chemical environments, including acid vapors and etchants. The increased length and ambient stability of the 17-AGNRs lead to their reliable integration into device architectures. As a proof of concept, we integrate 17-AGNRs into field-effect transistors (FET) with graphene electrodes and confirm that electronic transport occurs through the GNRs. This work demonstrates the feasibility of integrating narrow-bandgap GNRs into functional devices and contributes to advancing the development of carbon-based nanoelectronics.

Keywords: On-surface synthesis, Low bandgap graphene nanoribbons, scanning tunneling microscopy, raman spectroscopy, longitudinal compressive modes ,device integration

Introduction

Graphene nanoribbons (GNRs) are narrow, one-dimensional strips of graphene that exhibit unique physical properties compared to their two-dimensional counterpart. A key characteristic of GNRs is the emergence of a bandgap due to quantum confinement in one dimension, making them promising candidates for nanoelectronic applications.[1–4] Their electronic, magnetic, and optical properties can be further tailored through structural modifications, such as variations in edge geometry and ribbon width.

Depending on their edge geometry, GNRs can be classified into different groups, such as armchair (AGNR),[5,6] zigzag (ZGNR),[7,8] chevron (CGNR),[5,9] and chiral.[10] Among these, AGNRs have been the most extensively studied, both theoretically and experimentally, due to their width-tunable electronic properties and ambient stability, which make them suitable for integration into switching devices.[11] AGNRs are further classified into three families based on the number of carbon atoms across their width: $3p$, $3p + 1$, and $3p + 2$, where p is an integer. Within each family, the bandgap decreases monotonically with increasing width. However, because an atom-by-atom width increase alternates between these families, the overall bandgap variation is non-monotonic.[3,12–14] AGNRs belonging to the $3p + 2$ family have the narrowest electronic bandgap of these three families, which can result in more transparent Schottky barriers at the metal contact, thereby reducing contact resistance and improving device performance. To date, 5-, 7-, 9-, and 13-AGNRs have been successfully integrated into field effect transistor (FET) devices,[11,15–21] with 5-AGNRs being the only representative of the $3p + 2$ family.[22,23]

Due to the strong correlation between GNR geometry and electronic properties, synthesizing defect-free AGNRs with atomic-level precision is crucial for the development of devices with high reproducibility. On-surface synthesis (OSS) has emerged as a robust and reproducible bottom-up technique for achieving such control.[5,24,25] This approach relies on surface-assisted activation of specially designed organic precursors, which undergo polymerization via Ullmann-type coupling, followed by a cyclodehydrogenation reaction that planarizes the polymers, forming the final GNR structure.

Among the AGNRs accessible via OSS, 17-AGNRs represent a compelling candidate for device integration owing to their low electronic bandgap.[26] Density functional theory (DFT) predicts a bandgap of 0.14 eV, while experimental measurements on Au(111) by scanning tunneling spectroscopy indicate a gap of 0.19 eV.[26] While such a low bandgap could lead to lower resistance at the metal contacts, it also raises concerns regarding the ribbons' chemical stability and suitability for substrate transfer and device integration.[27,28] Moreover, based on standard electrode patterning techniques such as e-beam lithography, GNRs must be 15 nm or longer to bridge the source and drain with an effective contact area.[29]

In this work, we present an optimized growth protocol for synthesizing long and high-quality 17-AGNRs. By employing a high precursor coverage (near monolayer) and a gradual annealing process, we minimize defects and promote ribbon elongation. Scanning tunneling microscopy (STM) confirms that our approach yields 17-AGNRs with an average length of approximately 17 nm, while scanning tunneling spectroscopy (STS) reveals a bandgap of 0.45 eV. We perform Raman spectroscopy measurements to monitor the structural quality and ambient stability of the GNRs throughout their fabrication process: from growth in ultra-high vacuum to *ex-situ* transfer into the devices. We further conduct a combined experimental and theoretical Raman study to identify characteristic vibrational fingerprints of 17-AGNRs and assess their length distribution. Lastly, leveraging the improved structural quality and increased length of the ribbons, we fabricate and electrically characterize FET devices incorporating 17-AGNRs.

Results & discussion

Synthesis and length optimization of 17-AGNR

The synthesis and length optimization of 17-AGNRs were performed in ultra-high vacuum (UHV) and characterized by scanning tunneling microscopy (STM) (Figure 1a). The molecular precursor, **BADBB** (1,2-bis-(anthracenyl)-3,6-dibromobenzene), features a central benzene ring bonded to two anthracene units, which ultimately form the 17-carbon-wide GNR. **BADBB**

was synthesized *via* Suzuki coupling of 1,4-dibromo-2,3-diiodobenzene and anthracen-2-ylboronic acid as previously reported[26,30] and subsequently sublimated at 250 °C onto a clean Au(111) substrate in UHV at room temperature. A large-scale STM topography image of the surface after precursor deposition **BADBB** reveals approximately 70% of a monolayer coverage (Figure S1). The non-planar **BADBB** molecules self-assemble in large islands with different domain orientations. Within these assemblies (Figure S1b), the molecules adopt distinct geometries: a linear arrangement (with two opposite orientations) and an intermediate configuration (highlighted in green, blue, and yellow, respectively). At 77 K, STM lacks sufficient resolution due to molecular mobility, requiring support from density functional theory (DFT) simulations to discern the absorption configurations. Figure S1c shows the relaxed geometry of a single **BADBB** molecule and the corresponding STM simulation (left and right panels, respectively). Because of steric hindrance between the side groups, the anthracene units do not lie flat on the surface but adopt a tilted configuration.

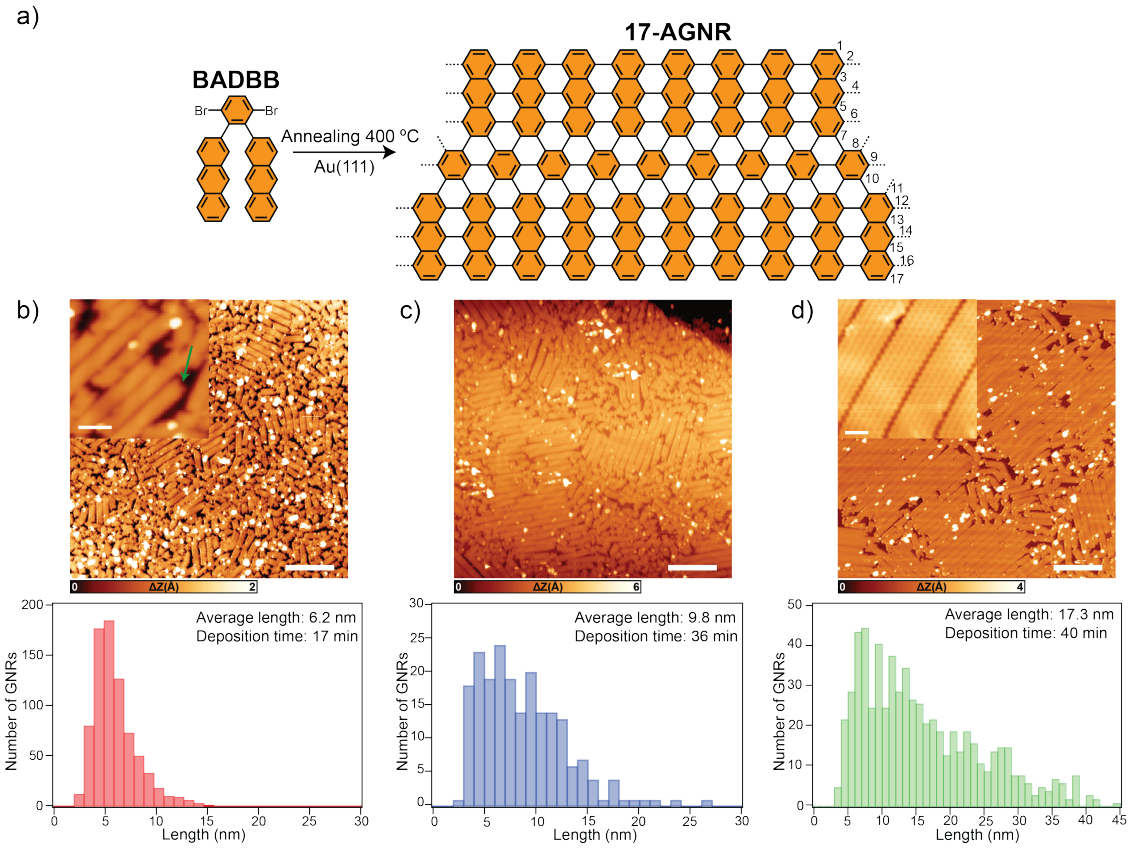


Figure 1: **On-surface synthesis and length optimization of 17-AGNR**. a) Chemical model of **BADBB** and final **17-AGNR**. b) STM image of 17-AGNRs after slow annealing ramp (deposition time: 17 min; scale bar: 10 nm; scanning parameters: -1.5 V and 30 pA). Inset: high resolution image showing the ends of the 17-AGNRs unit (scale bar: 10 nm scanning parameters: -1.0 V and 50 pA). The ribbons grow short (length distribution histogram at the bottom). c) STM image of 17-AGNR using higher initial coverage (deposition time: 36 min; scale bar: 10 nm; scanning parameters: -1.5 V and 30 pA). The ribbons grow longer with an average length of 9.8 nm. d) STM image of 17-AGNR using higher initial coverage (scale bar: 10 nm scanning parameters: -1.5 V and 30 pA). Inset: zoom-in image of 17-AGNR units with the expected width of 2.48 nm (scale bar: 1 nm). The ribbons grow longer than previous examples (average length of 17.3 nm with single ribbons exceeding 50 nm). STM measurements reported here have been performed at room temperature.

After deposition on Au(111), the samples were gradually annealed to induce, first, polymerization step and subsequently cyclodehydrogenation reactions, yielding 17-AGNRs. The coupling of **BADBB** radicals with confined movement on the growth substrate requires a 180° rotation between adjacent monomers, analogous to 9-AGNRs precursors.[31] Dehalogenation of bromine-containing precursors typically begins at 150 °C,[5,32] while cyclodehydrogenation—where H atoms are released to form C–C bonds— initiates above 350 °C. The formation of polymeric intermediates from the same precursor has been previously reported and thoroughly characterized via STM, showing the expected Ullmann-type coupling with alternating monomer orientation.[26] Capturing the polymeric intermediate via STM would have required interrupting the annealing process between 200–250 °C. Under these conditions, residual atomic hydrogen could passivate radical chain ends, leading to premature termination and reduced GNR length. To mitigate such passivation and preserve polymer growth, we implemented a slow temperature ramp of 2 °C/min from 150 °C to 400 °C, ensuring clear separation between dehalogenation and cyclodehydrogenation. This protocol was chosen to maximize GNR length and structural quality, at the cost of omitting direct STM imaging of the polymer in the present study.

Initial synthesis yielded relatively short GNRs averaging 6.2 nm in length, with unreacted fragments scattered across the surface (Figure 1b). To further promote the growth of longer GNRs, we increased the precursor deposition time to raise the initial **BADBB** coverage.[33] As shown in Figures 1c and d, this led to average GNR lengths of 9.8 nm and 17.3 nm, respectively. The longest GNRs were obtained when they grew in domains where they self-organized into parallel, ordered islands (Figure 1d)). This templating effect is known to enhance ribbon growth.[34] Moreover, higher coverage reduced the number of molecular fragments between GNRs, a possible cause of short units. The inset of Figure 1d shows a zoomed-in image confirming the expected width of 2.45 nm.[26]

Although the **BADBB** design suggests staggered termini, most 17-AGNRs instead exhibit two short protrusions at approximately 90° angles (green arrows in the insets of Figure 1b and S2a). To investigate these terminations, we prepared a low-coverage sample, yielding short GNRs where

both termini exhibit the aforementioned protrusions (Figure S2b). DFT calculations (Figure S2c) reveal that these arise from the rotation of the anthracene unit in the last molecular precursor segment and the subsequent formation of pentagons. This interpretation is supported by the close agreement between the experimental and simulated STM images in panels b and d in Figure S2, respectively. Once the anthracene units rotate and C-C bonds form, further precursor attachment is sterically hindered, effectively terminating GNR growth. This suggests that the longest 17-AGNRs are achieved under high precursor coverage and a slow annealing ramp, where the flipping of the anthracene units is strongly reduced.

For switching device applications, the electronic bandgap of GNRs is a critical parameter. Due to their large width, 17-AGNRs are expected to have smaller bandgaps than narrower AGNRs in the $3p + 2$ family. In addition to the 17-AGNRs, other members of the $3p + 2$ family have been experimentally characterized such as 5-,[22] 8-,[35] and 14-AGNRs.[36,37] Among these, only 5-AGNRs (bandgap dependent on the length[6,38]) were fabricated via controlled OSS approach on Au(111) and integrated into devices.[6,23,38] 8-AGNRs have been obtained in solution chemistry (optical gap of 0.52 eV[35]) or by lateral fusions of 3- and 5-AGNRs (reported bandgap of 2.3 eV[39]), while 14-AGNRs were synthesized by lateral fusion of two 7-AGNRs on Ag(111)[37] and on gold silicide (AuSIL), showing a bandgap of 0.2 eV.[36] Our DFT-PBE (Perdew-Burke-Ernzerhof) calculations (see Methods) for an infinitely long 17-AGNR predict a gas-phase bandgap of roughly 0.14 eV, significantly lower than for 7-AGNRs (1.58 eV) and 9-AGNRs (0.79 eV). While DFT underestimates absolute values, experimental bandgaps on Au(111) are reported as 2.3 eV for 7-AGNRs[40] and 1.4 eV for 9-AGNRs.[24] We characterized 17-AGNRs using scanning tunneling spectroscopy (STS) (Figure S3 a-c). The most intense points in the differential conductance ($\mathrm{d}I/\mathrm{d}V$) spectrum are selected to identify the different bands. The curve shows four main resonances: at -0.9 V (VB-1), -0.2 V(VB), 0.25 V(CB), and 1.3 V (CB+1). Conductance $\mathrm{d}I/\mathrm{d}V$maps of VB and CB show that, similarly to other AGNRs,[24,40] these are localized along the GNR length with higher intensity at the edges (Figure S3 d). From these measurements, we extract the experimental bandgap of 17-AGNRs on Au(111) to be approximately 0.45 eV, making it a promising candidate for high-

performance devices.

Raman characterization of 17-AGNR

To ensure successful device fabrication, it is crucial to evaluate the quality and robustness of the ribbons during substrate transfer and after device integration, as their structural integrity may be compromised during these steps. Owing to its versatility and high sensitivity to chemical structure, Raman spectroscopy has been extensively employed to characterize sp^2-hybridized carbon nanomaterials.[41–43] In graphene nanoribbons, it provides insights into GNR width,[27,41,42,44] edge structure,[41,45] length,[13] and alignment.[46] Furthermore, it enables the assessment of large-area uniformity and structural integrity after substrate transfer to dielectric layers and upon device nanofabrication steps.

The vibrational properties of GNRs give rise to four distinct spectral features: the longitudinal compressive mode (LCM), radial breathing-like mode (RBLM), CH/D modes, and the G mode.[13,47] The LCM appears at low frequencies (100 cm^{-1}), and its Raman shift is inversely proportional to the ribbon length. The RBLM is another low-frequency mode, and its Raman shift serves as a unique fingerprint of the nanoribbon width. For instance, the RBLMs of 5-, 7-, and 9-AGNRs have been experimentally measured at 531, 399, and 314 cm^{-1}, respectively.[48] The CH/D modes, found in the 1100–1500 cm^{-1} range, are characteristic of GNRs' one-dimensionality, with hydrogen-passivated edges breaking the lattice periodicity. Unlike graphene, where these modes emerge due to the presence of defects, they are intrinsic to GNR structures.[27,49] The G mode, centered near 1590 cm^{-1} arises from the collective in-plane vibrations of carbon atoms, and it is a signature peak of sp^2-hybridized carbon systems such as graphene and carbon nanotubes (CNTs). For GNRs, this mode consists of two components: the longitudinal-optical (LO) and the transverse-optical (TO) phonons, reflecting their distinct in-plane vibration directions.[13,22,27]

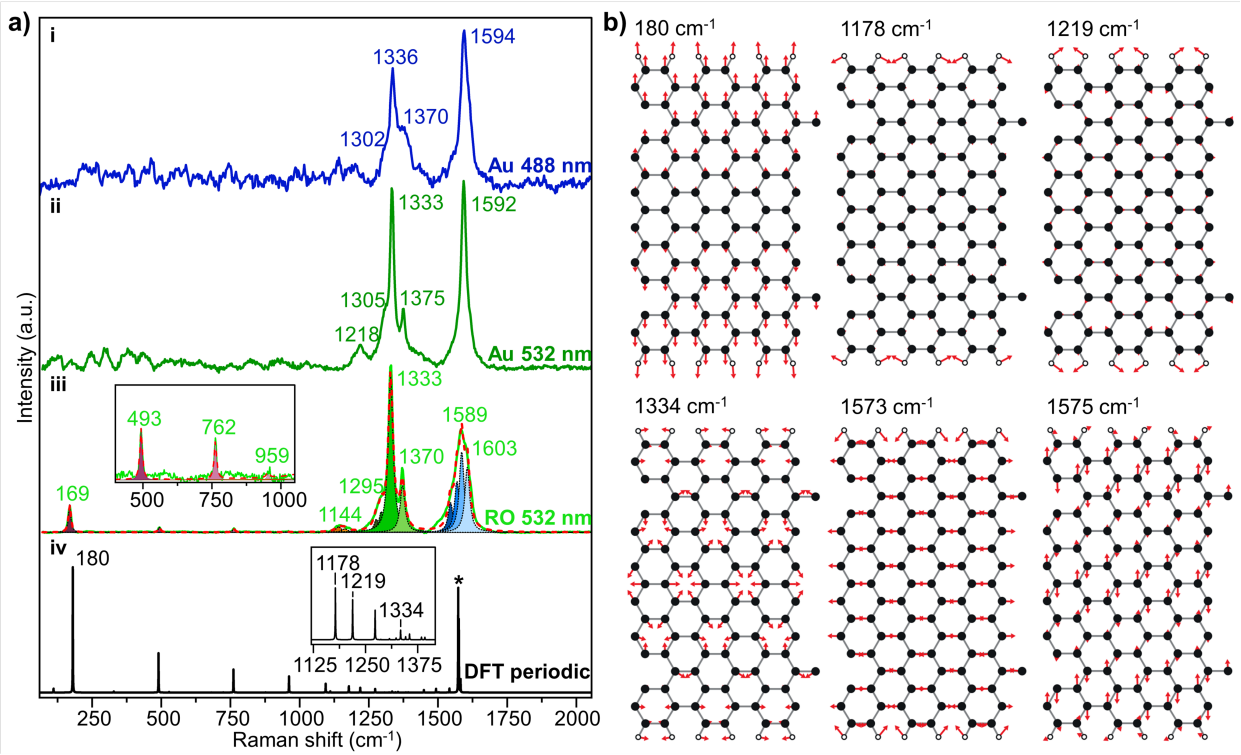


Figure 2: **Experimental and theoretical Raman spectra of 17-AGNRs**. a) Experimental Raman spectra on Au(111) using 488 nm (i. blue) and 532 nm (ii. green) laser wavelengths and on Raman-optimized (RO) substrate after substrate transfer using 532 nm laser wavelength (iii. light green) with its Lorentzian components, and a simulated Raman spectrum of a periodic 17-AGNR using DFT (iv. black). Four modes are simulated in the G peak: 1541, 1573, 1575, and 1581 cm^{-1}, with the LO mode centered at 1573 cm^{-1} being the most prominent, followed by the TO mode at 1575 cm^{-1} (marked with an asterisk). b) Normal mode analysis for RBLM, representative CH/D modes, and LO and TO phonon modes of the G peak obtained from DFT simulation.

To investigate the vibrational properties of 17-AGNRs, we measured Raman spectra on Au(111) and upon transfer to a Raman-optimized (RO) substrate (Al_2O_3(40 nm)/Au(80 nm)/SiO_2(285 nm)) using 488, 532, and 785 nm excitation laser wavelengths (λ_{ex}) with photon energies of 2.54, 2.33, and 1.58 eV, respectively. (Figures 2a and S4).

The Raman spectra of 17-AGNRs on Au(111) (Fig. 2a) reveal the characteristic CH/D peaks at ~1305, ~1333, and ~1375 cm^{-1} as well as a G peak at ~1592 cm^{-1}. Notably, a peak centered at 1218 cm^{-1} is observed upon λ_{ex} = 532 nm (2.33 eV) excitation but is absent at λ_{ex} = 488 nm (2.54 eV), indicating selective resonance with the 2.33 eV excitation.

To gain a deeper understanding of the origin of these vibrational modes, we performed periodic DFT calculations on an infinitely long 17-AGNR (Figure 2a panel iv). While the calculated intensities do not perfectly match experimental values, likely due to the absence of resonance effects and an accurate electron-phonon coupling description, the peak frequencies are in good agreement. Normal mode analysis (Figures 2b and S5) confirms that the peaks at 1305–1375 cm^{-1} arise from a mixture of carbon-hydrogen vibrations and ring breathing within the 1D GNR lattice. Additionally, it shows that the peak centered at 1218 cm^{-1} is associated with the carbon-hydrogen bending mode at the edges.

Low-frequency modes, such as the LCM and RBLM, can be suppressed on gold substrates due to their weak signal intensity and the substrate's influence on the specific collective motions characteristic of these modes. As demonstrated for other AGNRs,[48] transferring ribbons to an RO substrate enhances these modes by decoupling the ribbons from the metallic surface. Upon polymer-free transfer of 17-AGNRs (see Methods), we observe distinct low-frequency modes at 169, 493, 762, and 959 cm^{-1} with λ_{ex}=532 nm. These modes are associated with the RBLM and its overtones. When measured at λ_{ex}=488 nm, additional modes appear at the frequencies below 150 cm^{-1}, which will be discussed in the next section.

The presence of the RBLM and negligible changes in the overall peak positions before and after the transfer indicate that 17-AGNRs are stable in ambient conditions and their structure is preserved during the polymer-free transfer procedure.[27] Guided by our DFT and normal mode anal-

yses (Figures 2b and S5), we deconvoluted the experimental Raman spectra into their Lorentzian components (Figures 2a panel iii, S4 panels i, ii, iv, and v, and Table S2). The positions of the simulated spectra and the deconvoluted components agree relatively well, capturing the low-frequency and high-frequency modes.

Interestingly, the number and the widths of the constituent modes vary before and after the transfer (Figure 2a, Table S2). Focusing on the deconvoluted peaks from the spectra measured on Au(111) and on RO at λ_{ex}=532 nm (Table S2), CH/D modes centered at 1219, 1410, and 1437 cm^{-1} become less prominent, whereas the one at 1277 cm^{-1} newly appears after the transfer of the ribbons from gold to the RO substrate. In the G mode region, the splitting of the G peak into the different components is observed (Table S2). This is captured by both the deconvolution (1545, 1568, 1586, and 1606 cm^{-1}, on the RO substrate with λ_{ex}=532 nm) and normal mode analysis (1541, 1573, 1575, and 1581 cm^{-1}). Note that the intensities of CH/D modes are underestimated in the calculated Raman spectrum, likely due to the absence of resonance effects and precise electron-phonon coupling, which are not taken into account in this simulation. The modes at 1545, 1568, and 1606 cm^{-1} appear after the transfer in addition to the one at 1593 cm^{-1} on gold (1586 cm^{-1} on RO substrate). In addition, the width of the G mode centered at 1593 cm^{-1} decreases by 4 cm^{-1}, and those of the CH/D modes at 1305, 1333, and 1375 cm^{-1} increase by 3 cm^{-1} for the G modes. These may originate from multiple sources, such as GNRs interacting differently with different substrates (substrate effect) or variations in the length of the ribbons, as shown previously in 5-AGNRs where the Raman shift of the LO branch changes with GNR length, particularly for shorter ribbons.[22] In addition, discrepancies in the vibrational modes resolved at different excitation energies could be due to different modes getting excited differently depending on the excitation energy. Similar behaviors have already been observed for 5-, 7-, and 9-AGNRs.[22,27]

Length-dependent Raman studies

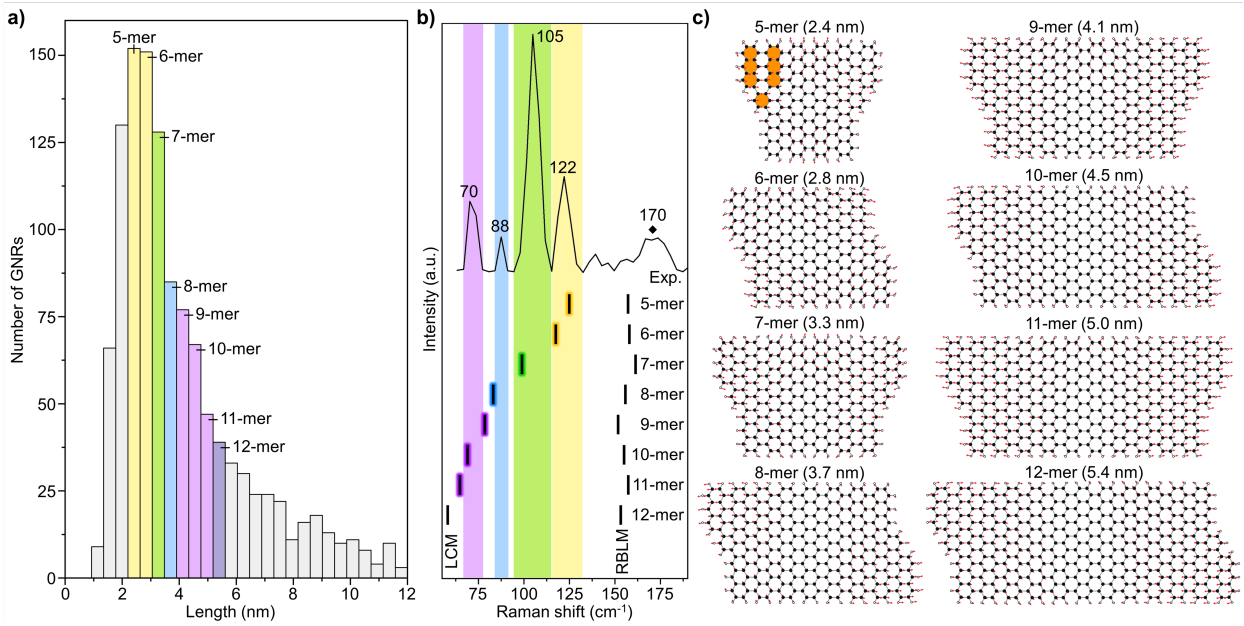


Figure 3: **Low frequency mode analysis.** a) Length distribution of the 17-AGNR sample measured by Raman. The histogram is truncated at 12 nm (bin size: 0.4 nm). 5- to 12-mers are highlighted in colors that represent the ranges of the LCM positions. b) Low-frequency region of the Raman spectrum of 17-GNRs on a 30 nm-thick Al_2O_3 dielectric layer measured at λ_{ex} = 488 nm (Exp., black). The RBLM from the experimental spectrum is marked with a black diamond (◆). Below, the theoretical positions of the LCMs and RBLM of 5- to 12-mer 17-AGNRs are marked with vertical lines. c) Atomic displacement profiles of LCMs for 5- to 12-mer 17-AGNRs modeled with REBOII. A monomer unit is highlighted in orange in a 5-mer 17-AGNR, and in the parentheses are the simulated sizes.

As observed in our scanning tunneling microscopy study of samples with varying initial precursor coverages, the final GNR length can differ significantly. To investigate this length variation using Raman spectroscopy[13,50] we synthesized a 17-AGNR sample with an average length of 4.5 nm (Figure 3a), comparable to the sample shown in Figure 1b. Raman spectra of this sample, measured with an excitation wavelength of λ_{ex} = 488 nm on a 20 nm-thick Al_2O_3 gate dielectric, reveal multiple peaks below 150 cm^{-1} (Figure 3b).

We observe four low-frequency peaks at 70 (violet), 88 (blue), 105 (green), and 122 (yellow) cm^{-1} (Figure 3b). To identify the origin of these modes and verify their correlation with GNR length, we employed the second-generation reactive empirical bond-order (REBOII) potential[51,52] to simulate the Raman spectra of 17-AGNRs with different lengths, ranging from 5 to 12 monomers (5- to 12-mer 17-AGNRs, Table S3). Unlike DFT analysis, which solves the Schrödinger equation through self-consistent iterations to model electronic interactions, REBOII employs predetermined mathematical functions to describe atomic interactions. This makes it a computationally efficient alternative that balances accuracy and resource demands for simulating vibrational modes in finite systems (see Methods). To evaluate the reliability of the REBOII model, we compared DFT- and REBOII-derived Raman spectra of 7- and 8-units long 17-AGNRs (7- and 8-mer 17-AGNRs). Figure S6 shows that while significant shifts occur in the high-frequency modes, the low-frequency modes exhibit negligible variation between the two methods. This confirms that the REBOII potential accurately captures the interatomic interactions between carbon atoms near equilibrium.

Our simulations indicate that the LCMs of 9-, 10-, and 11-units long 17-AGNRs (9-, 10-, and 11-mer 17-AGNRs, corresponding to lengths between 4 and 5 nm) contribute to the peak observed at 70 cm^{-1}. The histogram in Figure 3a shows a comparable amount of ribbons consisting of 9, 10, and 11 monomers, suggesting that their combination likely contributes to the rise of this peak. The peak at 88 cm^{-1} is assigned to the LCM of the 8-mer (3.7 nm) 17-AGNR, while the peaks at 105 cm^{-1} and 122 cm^{-1} are attributed to the LCMs of the 7-mer (3.3 nm) and 5- and 6-mers (2.4-2.8 nm) 17-AGNRs, respectively. The strong agreement between the Raman experimental data and simulation reflects the length distribution observed in the STM-derived histogram, particularly

in the sub-7 nm range where Raman spectroscopy is most sensitive to changes in ribbon length.[13]

Another notable feature is the broad RBLM peak (marked with a black diamond) observed in Figure 3b. We attribute this broadening to two factors: the variation in RBLM positions for 5- to 12-mer ribbons, which range from 154-162 cm^{-1} and the splitting of the RBLM into normal modes with diagonal atomic displacement in short GNRs[13] (Figure S7).

Finally, it is important to note that the LCMs corresponding to ribbons of length 5.4 nm or longer (ribbons with 12 or more monomer units) are not visible in this spectrum despite accounting for approximately 26.5% of the sample. This absence is likely due to the proximity of their vibrational frequencies to the Rayleigh scattering line, which limits their detectability in the Raman measurement.

Device integration and transport measurements

After demonstrating that 17-AGNRs can grow long enough to bridge source and drain and withstand the wet-transfer process, we integrated the GNRs into devices. The selected device structure is based on bottom electrodes made of graphene and defined using electron-beam lithography (EBL) and reactive ion etching (RIE), yielding nanogaps in the range of 15-20 nm.[29] The devices were fabricated as follows (more details in Methods): 1. Silicon/silicon dioxide (Si/SiO_2) with an oxide thickness of 285 nm served as the basis for the device fabrication. 2. A local gate is defined on top using standard EBL, covered using a ~20 nm thick Al_2O_3 gate dielectric. (Figure S8 and 4a inset) 3. Platinum lines on top serve as contacts to graphene electrodes. 4. Graphene electrodes are chosen due to their flatness and their proven capability to contact molecules[53] as well as graphene nanoribbons.[23,29,54,55]

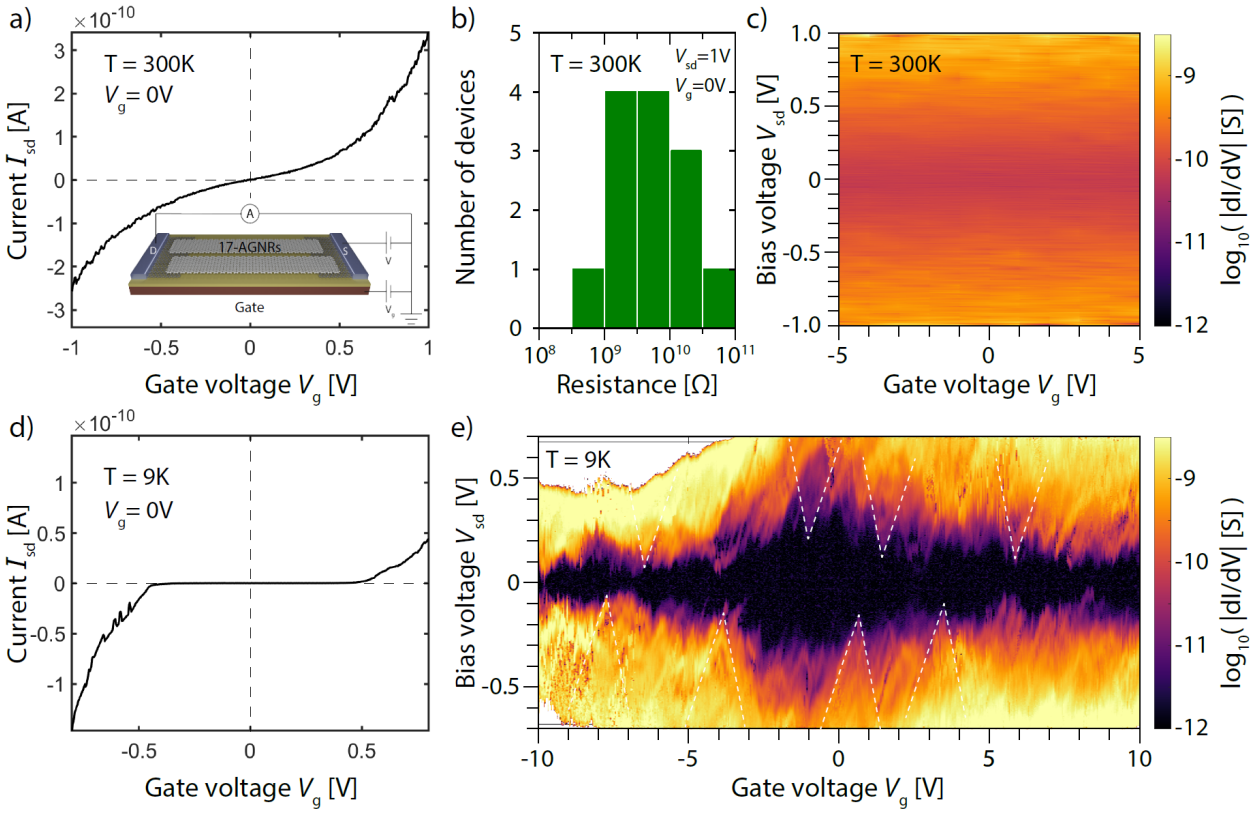


Figure 4: **Electrical characterization of 17-AGNR devices.** a) Current-voltage ($I - V$) trace of a typical device at room temperature. The inset shows the schematic of the device and measurement layout. b) Histogram of the room temperature device resistance for all 17-AGNR devices extracted at a bias voltage of 1 V due to the non-linearity of the I-V curve. c) Differential conductance dI/dVmap of the device in (a) at room temperature. d) $I - V$ trace of the same device as in (a) recorded at 9 K. e) dI/dVmap as a function of applied bias and gate voltages. The black region indicates the Coulomb blockade. White dashed lines are guides to the eye.

Room-temperature charge transport measurements reveal $I - V$ characteristics with source-drain currents reaching the nanoamperes range at an applied bias voltage of 1 V (Figure 4a). The curves are S-shaped, suggesting a Schottky-like barrier is present at the GNR/electrode interface. A thermal annealing step has been proposed by Braun et al. to improve the GNR/electrode interface.[29] For 9-AGNRs, this step leads to improved device performance, primarily due to local rearrangements and water removal at the GNR/graphene interface. However, such a step was not performed as a degradation of the 17-AGNRs was observed using Raman spectroscopy after annealing (Figure S9).

Figure 4b shows the histogram of the resistance values from 13 different 17-AGNR devices, extracted at an applied bias voltage of 1 V due to the nonlinearity of the $I - V$ characteristics. Although the device sample size may appear limited, it still represents a significant number of individual GNR devices characterized under identical fabrication and measurement conditions,[16,23,29] The average resistance of the 17-AGNR devices is 10.5 GOhm with a standard deviation of 16.7 GOhm. The considerable device-to-device variation is reflected in the high standard deviation and can be attributed to variations in GNR film quality (orientation of GNRs or coverage) and minor variations in electrodes (nanogap size, folds, wrinkles, or contaminants). Nevertheless, this is characteristic of nanodevice studies of this type, and the observed device behavior is consistent across all measured samples.

$I-V$s were recorded as a function of gate voltage, but little to no effect was observed (Figure 4c) for a representative device. This lack of gate dependence at room temperature is consistent with previous reports for other low-bandgap GNRs, for which no appreciable gate-dependent transport has been observed.[23,56]

At low temperature, the $I - V$ characteristics exhibit pronounced non-linearity with distinct step-like features (Figure 4d). These steps manifest as resonances in the differential conductance ($\mathrm{d}I/\mathrm{d}V$), indicating transport through quantized energy levels. Figure 4e shows a color map of the differential conductance as a function of bias and gate voltage. Regions of high and low conductance are clearly visible, reminiscent of Coulomb blockade and single-electron tunneling regimes,

respectively. However, despite the presence of sharp resonant features (white dashed lines), no clear Coulomb diamonds with well-defined crossing points are observed. This absence suggests that electronic transport occurs simultaneously through multiple conduction channels, implying that several 17-AGNRs contribute to the measured current. Given the graphene electrode geometry having widths of approximately 400 nm, it is likely that multiple 17-AGNRs bridge the electrodes both in parallel and in series. Additionally, localized states in the electrodes or charge traps within the oxide may further influence transport characteristics. Although such complexity prevents clear Coulomb diamond formation, these observations confirm that gate-tunable resonant transport can indeed occur at low temperatures, in contrast to room-temperature measurements.

This work demonstrates, for the first time, the successful integration of 17-AGNRs into device architectures. This represents a step toward the realization of low-voltage and potentially high-mobility graphene-based logic devices. While the transport performance of the 17-AGNR devices does not yet surpass that of previously reported GNR-FETs, particularly those based on longer 9-AGNRs with optimized short-channel geometries and strong metal contacts,[16] the present results elucidate key differences both in the GNRs and in the device architecture, accounting for the observed performance limitations. Here, the nanogap width (15–20 nm) is comparable to the average GNR length (∼17 nm), thereby limiting the achievable contact length and consequently the injection efficiency. In contrast, 9-AGNR-based devices have employed ribbons exceeding 50 nm, enabling more extended contacts (∼10–15 nm per electrode side) and superior electrostatic control.[16]

In addition to geometric limitations, structural imperfections such as atomic-scale "bite" defects[57,58] may further affect transport. Pizzochero et al. observe the emergence of pronounced localization on the sublattice closest to bite defects in 9-AGNRs, which in turn strongly affected the local density of states across the entire width, leading to a significant decrease in the conductance. In the case of the 17-AGNRs the presence of such defects likely contributes to the moderate device performance we observe in the present work. Despite these limitations, our results establish the feasibility of integrating 17-AGNRs into nanoelectronic devices and provide insight into the

interplay between ribbon quality, device geometry, and contact configuration. Future optimization of nanogap dimensions and contact engineering will be essential to unlock the full electronic potential of these narrow-bandgap semiconducting ribbons.

Conclusion

In this study, we optimized the on-surface synthesis conditions to produce long and high-quality 17-AGNRs by on-surface synthesis approach. We identified two key factors critical to achieving this: a gradual annealing process and a template-like effect induced by monomer clustering at high precursor coverage. Raman spectroscopy, performed both on the Au(111) growth substrate and after transfer to oxide-based device platforms, revealed that 17-AGNRs exhibit remarkable structural robustness despite their low bandgap. Furthermore, we demonstrate that Raman spectroscopy can be used to efficiently characterize GNR length by identifying several LCM modes. Owing to their optimized length and robustness, 17-AGNRs were successfully integrated into electronic devices. We investigated the transport properties of these GNRs in a FET geometry, where gate-independent transport was observed at room temperature, and sharp transport features were observed at cryogenic temperatures. Our findings highlight that 17-AGNRs, the widest AGNRs experimentally realized within the $3p + 2$ family, can be synthesized with significantly increased lengths and quality. This, combined with their structural robustness, allows the investigation of their electronic properties in an FET configuration.

Methods

Precursor synthesis The synthesis of **BADBB** was performed in solution through the Suzuki coupling of 1,4-dibromo-2,3-diiodobenzene and anthracen-2-ylboronic acid as previously described.[26,30] The final product quality was confirmed by Nuclear Magnetic Resonance (NMR) analysis.

Sample preparation The Au(111) single crystals (MaTeck GmbH) were prepared by iterative Ar^+ sputtering and annealing cycles. Prior to the sublimation of other species, the surface structure

and cleanliness were checked by STM imaging. The molecular precursor **BADBB** was loaded into quartz crucibles of a home-built evaporator and, after proper degassing, sublimated at approximately 250 °C onto a room-temperature substrate. After deposition, the precursors were annealed by applying a constant heating ramp of roughly 2 °C/min until 400 °C to favor the formation of long 17-AGNRs.

STM characterization STM measurements were performed with a commercial variable-temperature STM from Scienta Omicron operated at room temperature and base pressure below 5×10^{-11} mbar. In addition, due to their high mobility, measurements of **BADBB** precursors were acquired at LN_2 temperature (77 K), and spectroscopy data at LHe temperature (4.2 K). STM images were acquired in constant-current mode (overview and high-resolution imaging), dI/dVspectra were acquired in constant-height mode, and the feedback-loop off parameters are reported in the captions. Differential conductance dI/dVspectra were obtained with a lock-in amplifier. The data were processed with Wavemetrics Igor Pro software.

DFT-AiiDA DFT calculations were executed using the AiiDAlab applications,[59] based on AiiDA workchains[60] designed for the DFT code CP2K[61] (systems adsorbed on gold) and for the DFT code Quantum Espresso (bandstructure calculations).[62] Surface-adsorbate setups were modeled within a periodic slab scheme. The simulation cell included four Au atomic planes along the [111] orientation. Hydrogen atoms passivated one face of the slab to mitigate Au(111) surface states. A 40 Åvacuum layer was included to isolate the system from its periodic images along the axis orthogonal to the slab. Electronic wavefunctions were represented via TZV2P Gaussians basis sets for C and H, and DZVP for Au. Plane-waves basis set cutoff for the charge density was set at 600 Ry. Norm-conserving Goedecker–Teter–Hutter pseudopotentials were employed. The Perdew-Burke-Ernzerhof (PBE) generalized gradient approximation (GGA)[63] approximation for the exchange correlation functional was used, and Grimme's D3[64] van der Waals corrections were included. Au supercells varied in size depending on the adsorbates, ranging from 20.64×28.12 Å^2 (corresponding to 384 Au atoms) to 35.37×43.42 Å^2 (936 Au atoms). Geometry optimizations were performed with the bottom two atomic planes constrained while relaxing others until forces

were below 0.005 eV Å.

For the bandstructure calculations, ultrasoft pseudopotentials from the Standard solid-state pseudopotentials (SSSP)[65] were employed to model the ionic potentials. A cutoff of 50 Ry (400 Ry) was used for the plane wave expansion of the wave functions (charge density). The simulation cell contained 15 Å of vacuum in the non-periodic directions to minimize interactions among periodic replicas of the system. The thickness of the vacuum region, the sampling of the Brillouin zone (BZ), and the cutoff ensure the convergence of the computed band structures. The atomic positions of the ribbon atoms and the cell dimension along the ribbon axis were optimized until forces were lower than 0.002 eV/Åand the pressure in the cell was negligible. The band structures are aligned to the vacuum level computed from the average electrostatic potential in the vacuum region.

Substrate transfer The GNR/Au(111)/mica samples were placed on an HCl (*aq*). Within 15 minutes, the GNR/Au film cleaved from the mica substrate, after which the solution was diluted with water. The floating GNR/Au(111) film was then immersed in the diluted solution with the target substrate until it was fully submerged. The adhesion between the Au film and the target substrate was enhanced by applying a drop of ethanol to the Au film, followed by annealing at 100 °C for 10 minutes on a hot plate. The Au film was etched away using potassium iodide-based gold etchant (Sigma-Aldrich CAS No. 7681-11-0), resulting in GNRs on a target substrate.[27]

Raman spectroscopy After the sample was prepared and characterized using STM, it was transferred into a vacuum apparatus with optical access to the Raman microscope. Raman spectra were measured in back-scattering geometry using a Witec Alpha 300 R confocal Raman microscope, with 488, 532, and 785 nm excitations at 600 g/mm (488 and 532 nm) and 300 g/mm (785 nm) grating. For the respective excitations, the spectra were measured at 10, 5, and 2 mW with integration times of 10, 10, and 15 seconds, respectively, for the sample on a gold surface. The samples on RO were measured at 2, 5, and 10 mW, with integration times of 5, 1, and 5 seconds, respectively. The sample on a Al_2O_3 gate dielectric of a device was measured with 488 nm excitation at 1 mW for 10 seconds. The Raman spectra were recorded at 100 points and averaged. All spectra were collected using a 50x LD objective (Zeiss, NA = 0.55). All Raman spectra were collected at the

vacuum level ranging from 1-30 $\times$ 10^{-6} mbar. The data were processed with OriginPro.

Raman simulation The phonon calculation needed for Raman was carried out by Phonopy;[66] an open-source package to calculate phonons within the harmonic and quasi-harmonic approximation. Phonopy was paired with a calculator for the computation of the atomic forces obtained within a finite displacement scheme. For Raman calculation with REBO forces, the REBOII potential[52] was used for the calculation of the forces. REBOII potential is a classical hydrocarbon potential energy expression, which allows for bond making and breaking with appropriate changes in atomic hybridization.[51,52] Additionally, the bond polarizability model[67,68] was used for the calculation of the polarizability derivatives to obtain the Raman intensities. For Raman calculation of the periodic structure with DFT forces, structure relaxation was first performed by GPAW,[69,70] which is a DFT Python code based on the projector-augmented wave (PAW) method and the atomic simulation environment (ASE).[71] For relaxation, a plane-wave basis set was used with a plane-wave energy cutoff of 450 eV with a Γ-centered 9 $\times$ 1 $\times$ 1 Monkhorst-Pack Brillouin-zone sampling. Then, the phonon calculation was carried out by Phonopy using a 3 $\times$ 1 $\times$ 1 supercell with a displacement distance of 0.02 Å. The calculation of the force constants was performed by GPAW using the same plane-wave energy cutoff as used in the relaxation with a Γ-centered 4 $\times$ 1 $\times$ 1 Monkhorst-Pack sampling. The exchange-correlation functional used in these calculations was the GGA in the PBE formulation.[72]

Device fabrication Highly p-doped Si/SiO_2 (285 nm) serves as a base substrate for the device fabrication and serves as a global back gate (set to V_{gb} = 0 V). A thin gate electrode (Ti/Pd, 1/6 nm) is placed in the central region of the device and is covered by an atomic layer deposition (ALD)-grown dielectric layer (Al_2O_3, 20 nm). This allows for electrostatic gating of the 17-AGNRs. Palladium is chosen for the gate because it forms uniform, thin layers with low surface roughness.[73] Metal wires (Ti/Pt, 5/35 nm) serve as contact to the graphene electrodes. Platinum was chosen since it allows the transfer of GNRs grown on Au(111)/mica substrates, where the transfer process involves a gold etching step that does not attack platinum. In a last step, chemical vapor deposition (CVD)-grown graphene is placed on top and patterned using EBL. The cleanliness of the devices

is confirmed using atomic force microscopy, and electrical separation is performed using electrical transport characterization, as described below.

Transport All electronic measurements are performed under vacuum conditions ($<10^{-6}$ mbar) in a commercially available probe station (Model CRX-6.5K, Lake Shore Cryogenics). A data acquisition board (ADwin-Gold II, Jäger Computergesteuerte Messtechnik GmbH) is employed to apply and read the voltages from the $I-V$ converters (DDPCA-300, FEMTO Messtechnik GmbH and DELFT ELECTRONICS).

Author contribution

G.B.B. conceived and supervised the project. J.H.H., N.B., and G.B.B. performed the growth and characterization of GNRs. J.H.H. and N.B. analyzed the data. M.F. conducted Raman simulations under the supervision of V.M. O.B., M.S., and R.F., fabricated devices, and carried out transport measurements under the supervision of M.L.P. T.D. and H.H. synthesized the molecular precursors under the supervision of H.Y. and A.N. N.B. and C.P. performed the DFT calculations. J.H.H., N.B., and G.B.B. wrote the manuscript with input from all co-authors. G.B.B., P.R., R.F., and M.C. acquired funding and revised the manuscript.

Statement of conflict of interest

The authors declare no competing financial interest.

Supporting information

The Supporting Information is available online. BADBB-as deposited on Au(111); End-segments characterization of 17-AGNR; Electronic properties of 17-AGNR; Experimental Raman spectra of the 17-AGNRs; Raman normal mode analysis of a periodic structure from the DFT calculation; DFT and REBO II comparison of the peak positions; Positions and intensities of the

low-frequency modes calculated for 5- to 12-mer 17-AGNRs using REBOII; Device and graphene electrode separation assessment by scanning electron microscope (SEM) and atomic force microscopy (AFM); Raman characterization of transferred 17-AGNRs on device substrates; Peak information of the experimental Raman spectra; Peak information of the experimental Raman spectra after deconvolution; The lengths of the short 17-AGNRs simulated using REBOII.

Associated content

This manuscript has been previously submitted as a preprint. The citation for the preprint version is as follows: Jeong Ha Hwang; Nicolò Bassi; Mayada Fadel; Oliver Braun; Tim Dumslaff; Carlo Pignedoli; Michael Stiefel; Roman Furrer; Hironobu Hayashi; Hiroko Yamada; Akimitsu Narita; Klaus Müllen; Michel Calame; Mickael L. Perrin; Roman Fasel; Pascal Ruffieux; Vincent Meunier; Gabriela Borin Barin. Optimized Synthesis and Device Integration of Long 17-Atom-Wide Armchair Graphene Nanoribbons. arXiv preprint arXiv:2507.11307. https://arxiv.org/abs/2507.11307. 2025 July 15.

Acknowledgements

J.H.H., N.B., G.B.B., P.R., and R.F. greatly appreciate the financial support from the Werner Siemens Foundation (CarboQuant). O.B. and M.C. acknowledge funding by the EC H2020 FET Open project no. 767187 (QuIET). M.C. acknowledges funding by the Swiss National Science Foundation under the Sinergia grant no. 189924 (Hydronics). M.F. and V.M. acknowledge the support of the Focus Center at Rensselaer Polytechnic Institute, a NYS Department of Economic Development award (No. A21-0125-002 and RPI designation A50634.2326). M.L.P. acknowledges funding by the Swiss National Science Foundation (SNSF) under the Spark project no. 196795 and the Eccellenza Professorial Fellowship no. PCEFP2_203663. M.L.P. is also grateful for funding from the Swiss State Secretariat for Education, Research and Innovation (SERI) under contract number MB22.00076. H.H. and H.Y. are also grateful for JSPS KAKENHI grant no. JP20H02816

(H.H.), JP24K01576 (H.H.), JP20H05833 (H.Y.), and JP25K01751 (H.Y.). G.B.B., P.R., and R.F. acknowledge funding by the Swiss National Science Foundation under grant no. 212875 (SYNC) and the European Union Horizon 2020 research and innovation program under grant agreement no. 881603 (GrapheneFlagship Core 3). G.B.B. also greatly appreciates the European Union's Horizon Europe research and innovation program under grant agreement no. 101099098 (ATYPIQUAL) and the Swiss National Science Foundation grant no. 200021E-219172/1 (GRAAL). The authors are grateful for access to the Scanning Probe Microscopy User Lab at Empa for the AFM measurements, as well as the support provided by the staff of the Binnig and Rohrer Nanotechnology Center (BRNC) for device fabrication.

References

(1) Nakada, K.; Fujita, M.; Dresselhaus, G.; Dresselhaus, M. S. Edge state in graphene ribbons: Nanometer size effect and edge shape dependence. *Physical Review B* **1996**, *54*, 17954–17961.

(2) Zhou, Y.; Li, X.; Wang, Z.; Li, S.; Zu, X. Modulating the band gap of germanane nanoribbons for quantum well devices. *Physical Chemistry Chemical Physics* **2014**, *16*, 18029.

(3) Son, Y.-W.; Cohen, M. L.; Louie, S. G. Energy Gaps in Graphene Nanoribbons. *Physical Review Letters* **2006**, *97*.

(4) Lee, H.; Son, Y.-W.; Park, N.; Han, S.; Yu, J. Magnetic ordering at the edges of graphitic fragments: Magnetic tail interactions between the edge-localized states. *Physical Review B* **2005**, *72*.

(5) Cai, J.; Ruffieux, P.; Jaafar, R.; Bieri, M.; Braun, T.; Blankenburg, S.; Muoth, M.; Seitsonen, A. P.; Saleh, M.; Feng, X.; others Atomically precise bottom-up fabrication of graphene nanoribbons. *Nature* **2010**, *466*, 470–473.

(6) Kimouche, A.; Ervasti, M. M.; Drost, R.; Halonen, S.; Harju, A.; Joensuu, P. M.; Sainio, J.; Liljeroth, P. Ultra-narrow metallic armchair graphene nanoribbons. *Nature communications* **2015**, *6*, 10177.

(7) Ruffieux, P.; Wang, S.; Yang, B.; Sánchez-Sánchez, C.; Liu, J.; Dienel, T.; Talirz, L.; Shinde, P.; Pignedoli, C. A.; Passerone, D.; others On-surface synthesis of graphene nanoribbons with zigzag edge topology. *Nature* **2016**, *531*, 489–492.

(8) Blackwell, R. E.; Zhao, F.; Brooks, E.; Zhu, J.; Piskun, I.; Wang, S.; Delgado, A.; Lee, Y.-L.; Louie, S. G.; Fischer, F. R. Spin splitting of dopant edge state in magnetic zigzag graphene nanoribbons. *Nature* **2021**, *600*, 647–652.

(9) Teeter, J. D.; Zahl, P.; Mehdi Pour, M.; Costa, P. S.; Enders, A.; Sinitskii, A. On-Surface Synthesis and Spectroscopic Characterization of Laterally Extended Chevron Graphene Nanoribbons. *ChemPhysChem* **2019**, *20*, 2281–2285.

(10) Li, J.; Sanz, S.; Merino-Díez, N.; Vilas-Varela, M.; Garcia-Lekue, A.; Corso, M.; de Oteyza, D. G.; Frederiksen, T.; Peña, D.; Pascual, J. I. Topological phase transition in chiral graphene nanoribbons: from edge bands to end states. *Nature communications* **2021**, *12*, 5538.

(11) Mutlu, Z.; Lin, Y.; Barin, G.; Zhang, Z.; Pitner, G.; Wang, S.; Darawish, R.; Di Giovannantonio, M.; Wang, H.; Cai, J.; others Short-channel double-gate FETs with atomically precise graphene nanoribbons. 2021 IEEE International Electron Devices Meeting (IEDM). 2021; pp 37–4.

(12) Yang, L.; Park, C.-H.; Son, Y.-W.; Cohen, M. L.; Louie, S. G. Quasiparticle energies and band gaps in graphene nanoribbons. *Physical review letters* **2007**, *99*, 186801.

(13) Overbeck, J. et al. A Universal Length-Dependent Vibrational Mode in Graphene Nanoribbons. *ACS Nano* **2019**, *13*, 13083–13091.

(14) Saraswat, V.; Jacobberger, R. M.; Arnold, M. S. Materials Science Challenges to Graphene Nanoribbon Electronics. *ACS Nano* **2021**, *15*, 3674–3708.

(15) Bennett, P. B.; Pedramrazi, Z.; Madani, A.; Chen, Y.-C.; de Oteyza, D. G.; Chen, C.; Fischer, F. R.; Crommie, M. F.; Bokor, J. Bottom-up graphene nanoribbon field-effect transistors. *Applied Physics Letters* **2013**, *103*.

(16) Llinas, J. P.; Fairbrother, A.; Borin Barin, G.; Shi, W.; Lee, K.; Wu, S.; Yong Choi, B.; Braganza, R.; Lear, J.; Kau, N.; others Short-channel field-effect transistors with 9-atom and 13-atom wide graphene nanoribbons. *Nature communications* **2017**, *8*, 633.

(17) Jacobberger, R. M.; Arnold, M. S. High-Performance Charge Transport in Semiconducting Armchair Graphene Nanoribbons Grown Directly on Germanium. *ACS Nano* **2017**, *11*, 8924–8929.

(18) Ohtomo, M.; Sekine, Y.; Hibino, H.; Yamamoto, H. Graphene nanoribbon field-effect transistors fabricated by etchant-free transfer from Au(788). *Applied Physics Letters* **2018**, *112*.

(19) Zhang, J.; Qian, L.; Barin, G. B.; Daaoub, A. H. S.; Chen, P.; Müllen, K.; Sangtarash, S.; Ruffieux, P.; Fasel, R.; Sadeghi, H.; Zhang, J.; Calame, M.; Perrin, M. L. Contacting individual graphene nanoribbons using carbon nanotube electrodes. *Nature Electronics* **2023**, *6*, 572–581.

(20) Zhang, J.; Braun, O.; Barin, G. B.; Sangtarash, S.; Overbeck, J.; Darawish, R.; Stiefel, M.; Furrer, R.; Olziersky, A.; Müllen, K.; others Tunable Quantum Dots from Atomically Precise Graphene Nanoribbons Using a Multi-Gate Architecture. *Advanced electronic materials* **2023**, *9*, 2201204.

(21) Huang, W.; Braun, O.; Indolese, D. I.; Barin, G. B.; Gandus, G.; Stiefel, M.; Olziersky, A.; Müllen, K.; Luisier, M.; Passerone, D.; others Edge contacts to atomically precise graphene nanoribbons. *ACS nano* **2023**, *17*, 18706–18715.

(22) Borin Barin, G. et al. Growth Optimization and Device Integration of Narrow-Bandgap Graphene Nanoribbons. *Small* **2022**, *18*.

(23) El Abbassi, M.; Perrin, M. L.; Barin, G. B.; Sangtarash, S.; Overbeck, J.; Braun, O.; Lambert, C. J.; Sun, Q.; Prechtl, T.; Narita, A.; Müllen, K.; Ruffieux, P.; Sadeghi, H.; Fasel, R.; Calame, M. Controlled Quantum Dot Formation in Atomically Engineered Graphene Nanoribbon Field-Effect Transistors. *ACS Nano* **2020**, *14*, 5754–5762.

(24) Talirz, L.; Sode, H.; Dumslaff, T.; Wang, S.; Sanchez-Valencia, J. R.; Liu, J.; Shinde, P.; Pignedoli, C. A.; Liang, L.; Meunier, V.; others On-surface synthesis and characterization of 9-atom wide armchair graphene nanoribbons. *ACS nano* **2017**, *11*, 1380–1388.

(25) Houtsma, R. S. K.; de la Rie, J.; Stöhr, M. Atomically precise graphene nanoribbons: interplay of structural and electronic properties. *Chemical Society Reviews* **2021**, *50*, 6541–6568.

(26) Yamaguchi, J.; Hayashi, H.; Jippo, H.; Shiotari, A.; Ohtomo, M.; Sakakura, M.; Hieda, N.; Aratani, N.; Ohfuchi, M.; Sugimoto, Y.; Yamada, H.; Sato, S. Small bandgap in atomically precise 17-atom-wide armchair-edged graphene nanoribbons. *Communications Materials* **2020**, *1*.

(27) Borin Barin, G. et al. Surface-Synthesized Graphene Nanoribbons for Room Temperature Switching Devices: Substrate Transfer and *ex Situ* Characterization. *ACS Applied Nano Materials* **2019**, *2*, 2184–2192.

(28) Borin Barin, G.; Song, Y.; de Fátima Gimenez, I.; Souza Filho, A. G.; Barreto, L. S.; Kong, J. Optimized graphene transfer: Influence of polymethylmethacrylate (PMMA) layer concentration and baking time on graphene final performance. *Carbon* **2015**, *84*, 82–90.

(29) Braun, O. et al. Optimized graphene electrodes for contacting graphene nanoribbons. *Carbon* **2021**, *184*, 331–339.

(30) Dumslaff, T. Synthese und Charakterisierung neuartiger Graphennanostreifen und Graphenmoleküle mit Armlehnen- und Zickzack-Kanten. Ph.D. thesis, Johannes Gutenberg-Universität, Mainz, Germany, 2017.

(31) Talirz, L.; Ruffieux, P.; Fasel, R. On-Surface Synthesis of Atomically Precise Graphene Nanoribbons. *Advanced Materials* **2016**, *28*, 6222–6231.

(32) Di Giovannantonio, M.; Deniz, O.; Urgel, J. I.; Widmer, R.; Dienel, T.; Stolz, S.; Sánchez-Sánchez, C.; Muntwiler, M.; Dumslaff, T.; Berger, R.; others On-surface growth dynamics of graphene nanoribbons: the role of halogen functionalization. *ACS nano* **2018**, *12*, 74–81.

(33) Ishii, A.; Shiotari, A.; Sugimoto, Y. Quality control of on-surface-synthesised seven-atom wide armchair graphene nanoribbons. *Nanoscale* **2020**, *12*, 6651–6657.

(34) Moreno, C.; Paradinas, M.; Vilas-Varela, M.; Panighel, M.; Ceballos, G.; Peña, D.; Mugarza, A. On-surface synthesis of superlattice arrays of ultra-long graphene nanoribbons. *Chemical communications* **2018**, *54*, 9402–9405.

(35) Yao, X.; Zhang, H.; Kong, F.; Hinaut, A.; Pawlak, R.; Okuno, M.; Graf, R.; Horton, P. N.; Coles, S. J.; Meyer, E.; Bogani, L.; Bonn, M.; Wang, H. I.; Müllen, K.; Narita, A. N=8 Armchair Graphene Nanoribbons: Solution Synthesis and High Charge Carrier Mobility. *Angewandte Chemie International Edition* **2023**, *62*.

(36) Deniz, O.; Sánchez-Sánchez, C.; Dumslaff, T.; Feng, X.; Narita, A.; Müllen, K.; Kharche, N.; Meunier, V.; Fasel, R.; Ruffieux, P. Revealing the Electronic Structure of Silicon Intercalated Armchair Graphene Nanoribbons by Scanning Tunneling Spectroscopy. *Nano Letters* **2017**, *17*, 2197–2203.

(37) Huang, H.; Wei, D.; Sun, J.; Wong, S. L.; Feng, Y. P.; Neto, A. C.; Wee, A. T. S. Spatially resolved electronic structures of atomically precise armchair graphene nanoribbons. *Scientific reports* **2012**, *2*, 983.

(38) Lawrence, J.; Brandimarte, P.; Berdonces-Layunta, A.; Mohammed, M. S.; Grewal, A.; Leon, C. C.; Sanchez-Portal, D.; de Oteyza, D. G. Probing the magnetism of topological end states in 5-armchair graphene nanoribbons. *ACS nano* **2020**, *14*, 4499–4508.

(39) Sun, K.; Ji, P.; Zhang, J.; Wang, J.; Li, X.; Xu, X.; Zhang, H.; Chi, L. On-Surface Synthesis of 8-and 10-Armchair Graphene Nanoribbons. *Small* **2019**, *15*, 1804526.

(40) Ruffieux, P.; Cai, J.; Plumb, N. C.; Patthey, L.; Prezzi, D.; Ferretti, A.; Molinari, E.; Feng, X.; Müllen, K.; Pignedoli, C. A.; others Electronic structure of atomically precise graphene nanoribbons. *ACS nano* **2012**, *6*, 6930–6935.

(41) Liu, D.; Daniels, C.; Meunier, V.; Every, A. G.; Tománek, D. In-plane breathing and shear modes in low-dimensional nanostructures. *Carbon* **2020**, *157*, 364–370.

(42) Verzhbitskiy, I. A.; Corato, M. D.; Ruini, A.; Molinari, E.; Narita, A.; Hu, Y.; Schwab, M. G.; Bruna, M.; Yoon, D.; Milana, S.; Feng, X.; Müllen, K.; Ferrari, A. C.; Casiraghi, C.; Prezzi, D. Raman Fingerprints of Atomically Precise Graphene Nanoribbons. *Nano Letters* **2016**, *16*, 3442–3447.

(43) Thapliyal, V.; Alabdulkarim, M. E.; Whelan, D. R.; Mainali, B.; Maxwell, J. L. A concise review of the Raman spectra of carbon allotropes. *Diamond and Related Materials* **2022**, *127*, 109180.

(44) Vandescuren, M.; Hermet, P.; Meunier, V.; Henrard, L.; Lambin, P. Theoretical study of the vibrational edge modes in graphene nanoribbons. *Physical Review B* **2008**, *78*.

(45) Kim, J.; Lee, N.; Min, Y. H.; Noh, S.; Kim, N.-K.; Jung, S.; Joo, M.; Yamada, Y. Distinguishing Zigzag and Armchair Edges on Graphene Nanoribbons by X-ray Photoelectron and Raman Spectroscopies. *ACS Omega* **2018**, *3*, 17789–17796.

(46) Darawish, R.; Overbeck, J.; Müllen, K.; Calame, M.; Ruffieux, P.; Fasel, R.; Borin Barin, G.

Quantifying alignment and quality of graphene nanoribbons: A polarized Raman spectroscopy approach. *Carbon* **2024**, *218*, 118688.

(47) Wu, J.-B.; Lin, M.-L.; Cong, X.; Liu, H.-N.; Tan, P.-H. Raman spectroscopy of graphene-based materials and its applications in related devices. *Chemical Society Reviews* **2018**, *47*, 1822–1873.

(48) Overbeck, J. et al. Optimized Substrates and Measurement Approaches for Raman Spectroscopy of Graphene Nanoribbons. *Physica Status Solidi (b)* **2019**, *256*.

(49) Eckmann, A.; Felten, A.; Verzhbitskiy, I.; Davey, R.; Casiraghi, C. Raman study on defective graphene: Effect of the excitation energy, type, and amount of defects. *Physical Review B* **2013**, *88*.

(50) Borin Barin, G.; Di Giovannantonio, M.; Lohr, T. G.; Mishra, S.; Kinikar, A.; Perrin, M. L.; Overbeck, J.; Calame, M.; Feng, X.; Fasel, R.; Ruffieux, P. On-surface synthesis and characterization of teranthene and hexanthene: ultrashort graphene nanoribbons with mixed armchair and zigzag edges. *Nanoscale* **2023**, *15*, 16766–16774.

(51) Brenner, D. W. Empirical potential for hydrocarbons for use in simulating the chemical vapor deposition of diamond films. *Phys. Rev. B* **1990**, *42*, 9458–9471.

(52) Brenner, D. W.; Shenderova, O. A.; Harrison, J. A.; Stuart, S. J.; Ni, B.; Sinnott, S. B. A second-generation reactive empirical bond order (REBO) potential energy expression for hydrocarbons. *Journal of Physics: Condensed Matter* **2002**, *14*, 783.

(53) El Abbassi, M.; Sangtarash, S.; Liu, X.; Perrin, M. L.; Braun, O.; Lambert, C.; van der Zant, H. S. J.; Yitzchaik, S.; Decurtins, S.; Liu, S.-X.; Sadeghi, H.; Calame, M. Robust graphene-based molecular devices. *Nature Nanotechnology* **2019**, *14*, 957–961.

(54) Niu, W. et al. Exceptionally clean single-electron transistors from solutions of molecular graphene nanoribbons. *Nature Materials* **2023**, *22*, 180–185.

(55) Chen, Q.; Lodi, A.; Zhang, H.; Gee, A.; Wang, H. I.; Kong, F.; Clarke, M.; Edmondson, M.; Hart, J.; O'Shea, J. N.; others Porphyrin-fused graphene nanoribbons. *Nature Chemistry* **2024**, *16*, 1133–1140.

(56) Sun, Q.; Gröning, O.; Overbeck, J.; Braun, O.; Perrin, M. L.; Borin Barin, G.; El Abbassi, M.; Eimre, K.; Ditler, E.; Daniels, C.; others Massive Dirac fermion behavior in a low bandgap graphene nanoribbon near a topological phase boundary. *Advanced materials* **2020**, *32*, 1906054.

(57) Pizzochero, M.; Barin, G. B.; Čerņevičs, K.; Wang, S.; Ruffieux, P.; Fasel, R.; Yazyev, O. V. Edge Disorder in Bottom-Up Zigzag Graphene Nanoribbons: Implications for Magnetism and Quantum Electronic Transport. *The Journal of Physical Chemistry Letters* **2021**, *12*, 4692–4696.

(58) Pizzochero, M.; Čerņevičs, K.; Borin Barin, G.; Wang, S.; Ruffieux, P.; Fasel, R.; Yazyev, O. V. Quantum electronic transport across 'bite' defects in graphene nanoribbons. *2D Materials* **2021**, *8*, 035025.

(59) Yakutovich, A. V.; Eimre, K.; Schütt, O.; Talirz, L.; Adorf, C. S.; Andersen, C. W.; Ditler, E.; Du, D.; Passerone, D.; Smit, B.; others AiiDAlab–an ecosystem for developing, executing, and sharing scientific workflows. *Computational Materials Science* **2021**, *188*, 110165.

(60) Pizzi, G.; Cepellotti, A.; Sabatini, R.; Marzari, N.; Kozinsky, B. AiiDA: automated interactive infrastructure and database for computational science. *Computational Materials Science* **2016**, *111*, 218–230.

(61) Hutter, J.; Iannuzzi, M.; Schiffmann, F.; VandeVondele, J. cp2k: atomistic simulations of condensed matter systems. *Wiley Interdisciplinary Reviews: Computational Molecular Science* **2014**, *4*, 15–25.

(62) Giannozzi, P.; Baroni, S.; Bonini, N.; Calandra, M.; Car, R.; Cavazzoni, C.; Ceresoli, D.; Chiarotti, G. L.; Cococcioni, M.; Dabo, I.; others QUANTUM ESPRESSO: a modular and

open-source software project for quantumsimulations of materials. *Journal of physics: Condensed matter* **2009**, *21*, 395502.

(63) Perdew, J. P.; Burke, K.; Ernzerhof, M. Generalized gradient approximation made simple. *Physical review letters* **1996**, *77*, 3865.

(64) Grimme, S.; Antony, J.; Ehrlich, S.; Krieg, H. A consistent and accurate ab initio parametrization of density functional dispersion correction (DFT-D) for the 94 elements H-Pu. *The Journal of chemical physics* **2010**, *132*.

(65) Lejaeghere, K.; Bihlmayer, G.; Björkman, T.; Blaha, P.; Blügel, S.; Blum, V.; Caliste, D.; Castelli, I. E.; Clark, S. J.; Dal Corso, A.; others Reproducibility in density functional theory calculations of solids. *Science* **2016**, *351*, aad3000.

(66) Togo, A.; Tanaka, I. First principles phonon calculations in materials science. *Scripta Materialia* **2015**, *108*, 1–5.

(67) Guha, S.; Menéndez, J.; Page, J. B.; Adams, G. B. Empirical bond polarizability model for fullerenes. *Phys. Rev. B* **1996**, *53*, 13106–13114.

(68) Saito, R.; Furukawa, M.; Dresselhaus, G.; Dresselhaus, M. S. Raman spectra of graphene ribbons. *Journal of Physics: Condensed Matter* **2010**, *22*, 334203.

(69) Mortensen, J. J.; Hansen, L. B.; Jacobsen, K. W. Real-space grid implementation of the projector augmented wave method. *Phys. Rev. B* **2005**, *71*, 035109.

(70) Enkovaara, J. et al. Electronic structure calculations with GPAW: a real-space implementation of the projector augmented-wave method. *Journal of Physics: Condensed Matter* **2010**, *22*, 253202.

(71) Hjorth Larsen, A. et al. The atomic simulation environment—a Python library for working with atoms. *Journal of Physics: Condensed Matter* **2017**, *29*, 273002.

(72) Perdew, J. P.; Burke, K.; Ernzerhof, M. Generalized Gradient Approximation Made Simple. *Phys. Rev. Lett.* **1996**, *77*, 3865–3868.

(73) Nazarpour, S.; Cirera, A.; Varela, M. Material properties of Au–Pd thin alloy films. *Thin Solid Films* **2010**, *518*, 5715–5719.